The International Journal of Advanced Manufacturing Technology (2018) 98:373–383
https://doi.org/10.1007/s00170-018-2271-8

ORIGINAL ARTICLE

Numerical study on flow characteristics and impact erosion in ultrasonic assisted waterjet machining

Zhe Lv[1] · Rongguo Hou[1] · Yebing Tian[1] · Chuanzhen Huang[2] · Hongtao Zhu[2]

Received: 1 December 2017 / Accepted: 4 June 2018 / Published online: 9 June 2018
© Springer-Verlag London Ltd., part of Springer Nature 2018

Abstract
A 3D numerical model was established to study the flow field characteristics and particle erosion in ultrasonic vibration-assisted abrasive waterjet machining by using computational fluid dynamics. The vibration of target is realized by using user-defined functions and dynamic meshing. The trajectories of abrasive particles dispersed in fluid flow are calculated by employing discrete phase model. The material removal on impacted surface was considered by an erosion rate model. The results indicated that the erosion rate at center area of impacted zone is lower than that at peripheral area, which is owing to the influence of stagnation zone. The variation of pressure value at the impacted surface is related to the vibrating movement of workpiece. Due to the weakening of stagnation effect, the pressure value decreases with a reduction of impact angle. Moreover, it was found that the erosion rate induced by particle impact on target surface is increased when vibration is applied. The influence of ultrasonic vibration on erosion rate is more significant at lower impact angle.

Keywords Computational fluid dynamics · Abrasive waterjet · Impact fluid field · Ultrasonic assisted machining

1 Introduction

Abrasive waterjet technology is a special processing method using hard particles as microtools and pressurized water as accelerating medium. Due to low thermal damage and high flexibility, it is suitable for processing components made of hard brittle materials such as ceramics and glasses [1–3]. In abrasive waterjet machining, material on the workpiece surface is repeatedly impacted by plenty of particles. The detachment and removal will occur after the failure of material. This process is commonly termed as erosion or wear. Finnie [4] did some fundamental studies on detailed mechanism of abrasive particle erosion on ductile materials. He proposed a microcutting model to interpret the erosion process. For brittle materials, failure caused by successive particle impacts mainly manifests as intersection of fractures. Evans et al. [5] used the fracture mechanics of dynamic indentation to investigate the crack initiation and propagation involved in abrasive erosion of brittle materials. However, nominally, brittle materials can also behave some characteristics of ductile removal when the indentation deformation is small enough, which is observed by Sheldon and Finnie [6]. Zhu et al. [7] adjusted the working parameters in abrasive waterjet such as using small abrasive diameters and low water pressure to confine the kinetic energy of particles and realized the ductile removal of brittle materials for the purpose of surface polishing. Nevertheless, the processing efficiency is relatively lower.

Many researchers have implemented the ultrasonic vibration into the traditional machining methods for improving the processing efficiency and quality [8, 9]. Liang et al. [10] carried out ultrasonic assisted grinding of monocrystal sapphire and found that the sharp cutting period was longer and the grinding force was lower, which are good for a smoother work surface. Li et al. [11] modeled the grinding force in ultrasonic assisted grinding and found that the vibration amplitude has a significant influence on reducing the subsurface damage. Xiao et al. [12] conducted

✉ Zhe Lv
lzjslyz@126.com

[1] School of Mechanical Engineering, Shandong University of Technology, Zibo 255000, China

[2] Center for Advanced Jet Engineering Technologies (CaJET), Key Laboratory of High-efficiency and Clean Mechanical Manufacture (Ministry of Education), School of Mechanical Engineering, Shandong University, Jinan 250061, China

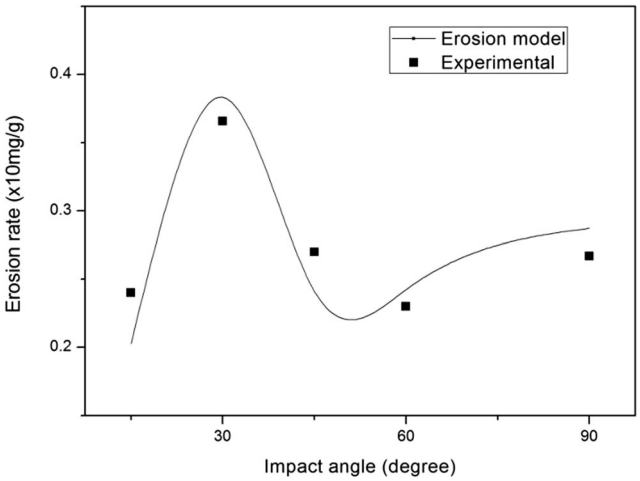

Fig. 1 The erosion rates predicted by the present model compared with experimental results

ultrasonic assisted side grinding of zirconia ceramics and found that ultrasonic vibration can increase the critical depth for ductile grinding and reduce the grinding forces. Therefore, it is reasonable to introduce ultrasonic vibration into abrasive waterjet machining for the purpose of increasing processing efficiency. The present authors have carried out some preliminary tests on machining of aluminum nitride components, and the results indicated that the ultrasonic vibration can effectively increase the material removal rate of abrasive waterjet [13, 14]. Qi et al. [15] utilized ultrasonic assisted slurry jet in microchanneling of glasses samples and found that the ultrasonic vibration can improve the direct impact and viscous flow induced erosion.

The motions of abrasive particles are affected by the containing water flow and can be hardly observed and measured. Therefore, numerical simulation is commonly used to investigate the flow field containing disperse particles. Nouraei et al. [16] studied the relations between impact angle and erosion rate in abrasive slurry jet machining by using computational fluid dynamics (CFD). The particle trajectories were obtained to calibrate the local impact angles of particles. Kowsari et al. [17] used a CFD model to investigate the specific erosion rate dependence on particle impact angle and velocity. Moreover, he utilized the relations obtained by CFD to predict the erosive profiles in abrasive slurry jet machining of sintered ceramics. Qi et al. [18] modeled the impinging flow field of abrasive slurry jet on a vibration specimen and found that the erosion rate is enhanced due to the improved ductile removal.

In the present study, a three-dimensional flow field model of ultrasonic vibration-assisted abrasive waterjet machining is established by using CFD. The vibration of target is realized by using user defined functions and dynamic grid methods. The motions of abrasive particles dispersed in fluid flow are calculated through using discrete phase model. Effects of different parameters such as impact angle and vibration condition on the flow field characteristics. Moreover, the erosion rate with respect to ultrasonic vibration is investigated by employing an impact erosion model.

2 Modeling

2.1 Governing equations

The abrasive waterjet is a flow with mixed phases including water, entrained air, and abrasive particles. The volume fractions of water and air are assumed to be continuous functions of space and time, and their sum is equal to unity. Conservation equations for air and water phases are derived

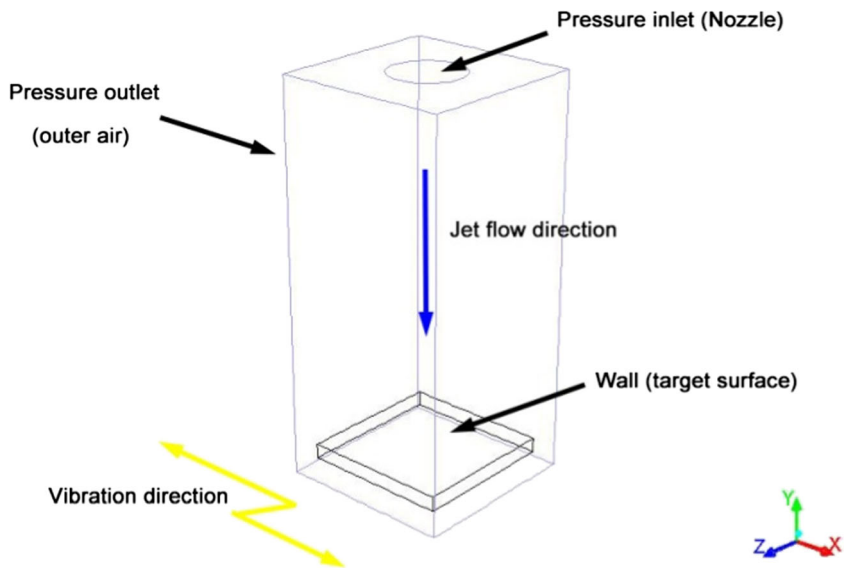

Fig. 2 Geometry of computational domain of flow field (impact angle = 90°)

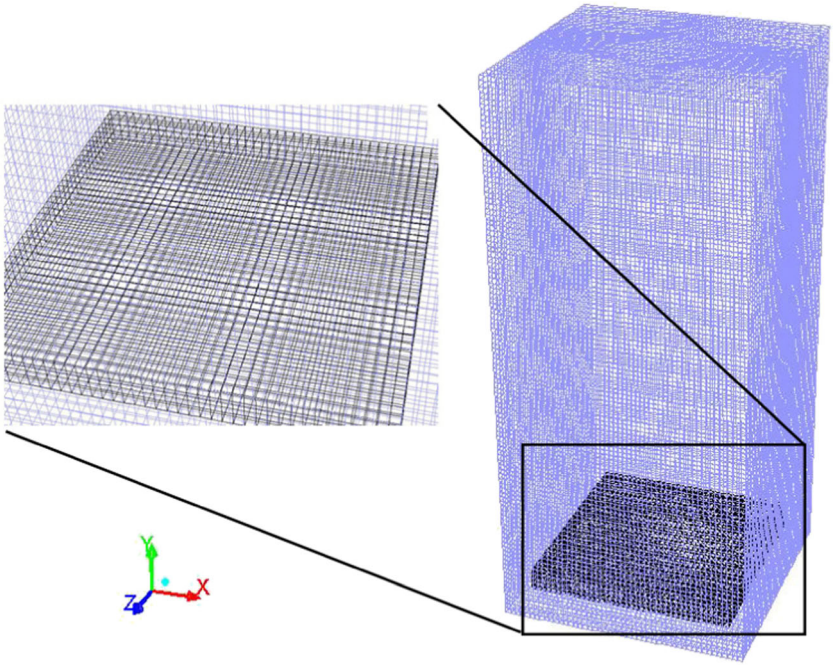

Fig. 3 Mesh model of impact flow field (impact angle = 90°)

to obtain a set of equations. A single set of momentum equations is shared by two phases [19]:

$$\frac{\partial}{\partial t}(\rho v) + \nabla\cdot(\rho v v) = -\nabla p + \nabla\cdot\left[\mu\left(\nabla v + \nabla v^{T}\right)\right] + \rho g + F \tag{1}$$

where p is the static pressure, v is the velocity, μ is the molecular viscosity, ρ is the density, g is the gravitational acceleration, and F is the external body force. As heat transfer or compressibility is not considered in this study, additional equations for energy conservation are not solved.

The flow field of abrasive waterjet with high Reynolds number is characterized by small-scale and high-frequency fluctuations of flow quantities. Therefore, transport equations relating turbulence also should be considered. Reynolds-averaged Navier-Stokes equations which govern the transport of averaged flow quantities can be used to model the

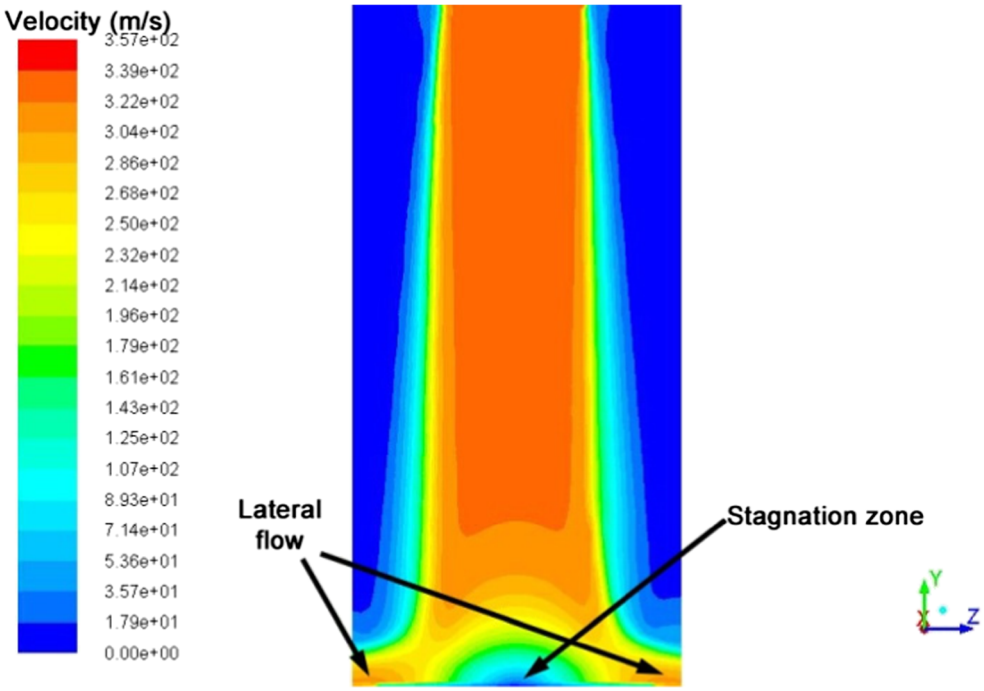

Fig. 4 Flow structure and impinging fluid field of abrasive waterjet (impact angle = 90°)

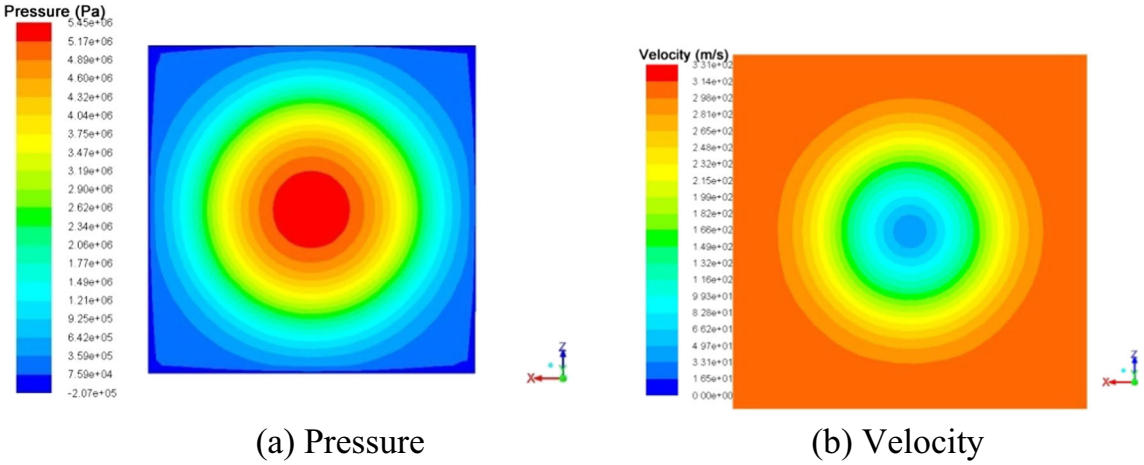

Fig. 5 Distributions of flow field on the impacted surface (impact angle = 90°). **a** Pressure. **b** Velocity

turbulence as well as reduce computational resources. An improved two-equation model, RNG k-ε model was utilized to describe the transportation of turbulent energy and its dissipation rate [20]:

$$\frac{\partial(\rho k)}{\partial t}+\frac{\partial(\rho u_i k)}{\partial x_i}=\frac{\partial}{\partial x_j}\left[\alpha_k \mu_e \frac{\partial k}{\partial x_j}\right]+G_k+G_b-\rho\varepsilon+S_k \quad (2)$$

$$\frac{\partial(\rho\varepsilon)}{\partial t}+\frac{\partial(\rho u_i \varepsilon)}{\partial x_i}=\frac{\partial}{\partial x_j}\left[\alpha_\varepsilon \mu_e \frac{\partial \varepsilon}{\partial x_j}\right] + C_{1\varepsilon}\frac{\varepsilon}{k}(G_k+C_{3\varepsilon}G_b)-C_{2\varepsilon}\rho\frac{\varepsilon^2}{k}+S_\varepsilon \quad (3)$$

where μ_e is the effective viscosity, G_k represents the generation of turbulence kinetic energy due to the mean velocity gradients, G_b is the generation of turbulent kinetic energy due to the buoyancy, $C_{1\varepsilon}$, $C_{2\varepsilon}$, and $C_{3\varepsilon}$ are constants, α_k and α_ε are inverse effective Prandtl numbers for k and ε, respectively, S_k and S_ε are source terms. The effect of swirl on turbulence is included in RNG model, and therefore enhancing the accuracy.

The abrasive particle is immersed in the gas-liquid flow and has a particular inertial response to and interaction with the particular field. The volume fraction occupied by the particles is relatively low. Therefore, discrete phase model is utilized to calculate the Lagrangian trajectories of abrasive particles and the interaction with the continuous gas-liquid flow field. The formulation used to calculate the trajectory of discrete phase includes the inertia, hydrodynamic drag, and gravity [21]:

$$\frac{du_p}{dt}=F_D(u-u_p)+\frac{g\left(\rho_p-\rho\right)}{\rho_p}+F_x \quad (4)$$

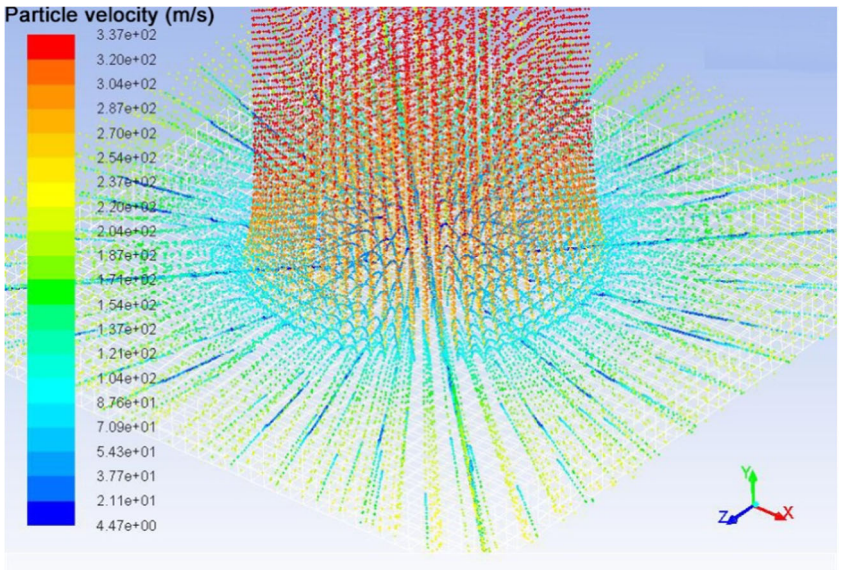

Fig. 6 Particle trajectories in the flow field of impinging waterjet (impact angle = 90°)

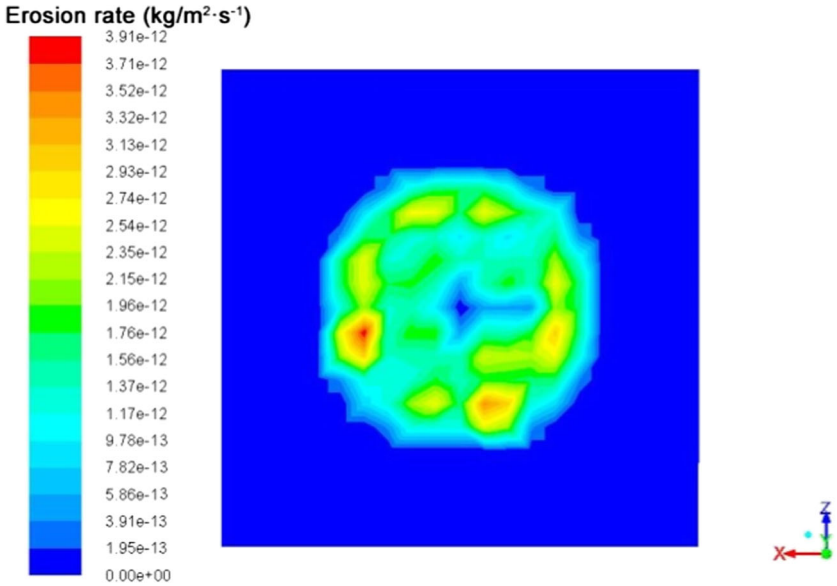

Fig. 7 Erosion rate of particles on the impacted workpiece (impact angle = 90°)

where u_p is the velocity of discrete phase, u is the velocity of carrier phase, $F_D(u\text{-}u_p)$ is the hydrodynamic drag, g is the gravitational acceleration, ρ_p is the density of discrete phase, ρ is the density of carrier phase, and F_x is the external load induced by inertia and pressure gradient of fluid. The drag force can be expressed as follows:

$$F_D = \frac{18u}{\rho_p d_p^2} \cdot \frac{C_D \mathrm{Re}}{24} \tag{5}$$

where d_p is the diameter of the abrasive particle, C_D is drag coefficient, and Re is the relative Reynolds number.

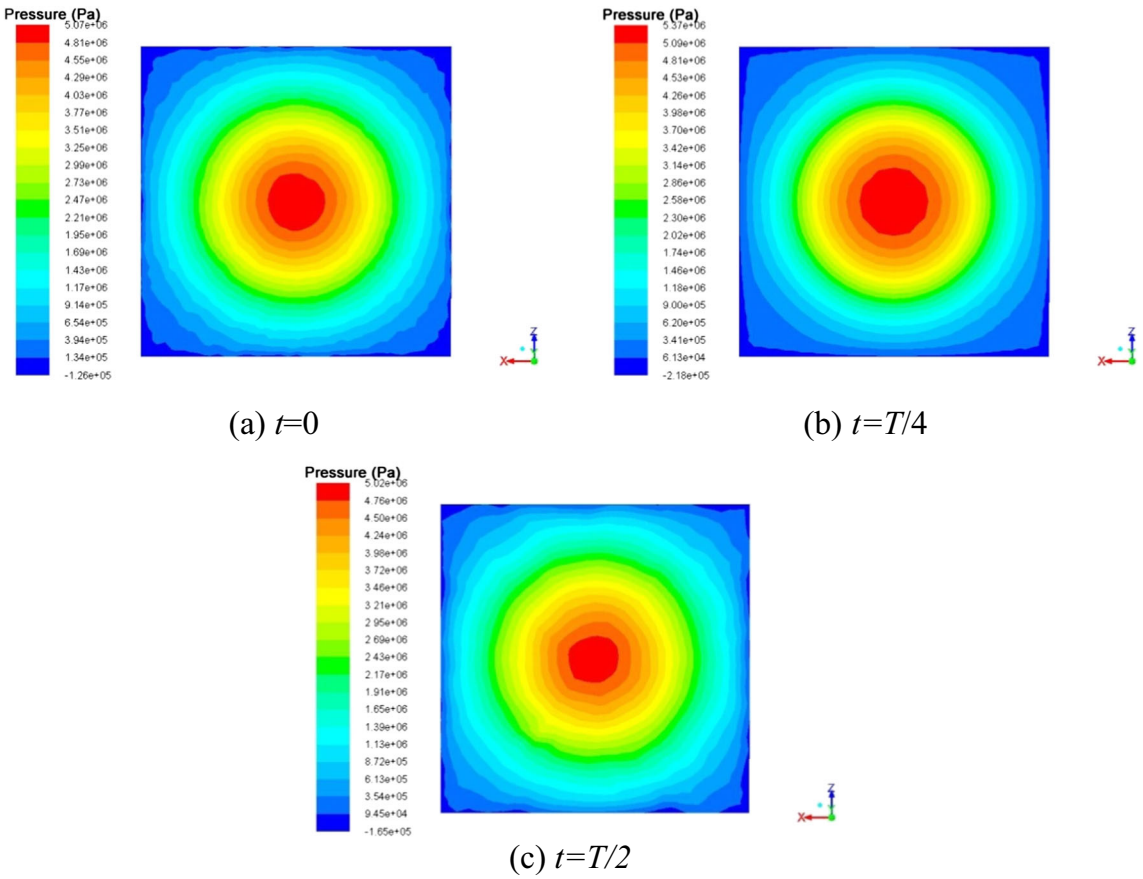

(a) t=0 (b) t=T/4

(c) t=T/2

Fig. 8 Pressure distribution of flow fields on impacted surfaces at different moment during a vibration period. **a** $t = 0$. **b** $t = T/4$. **c** $t = T/2$

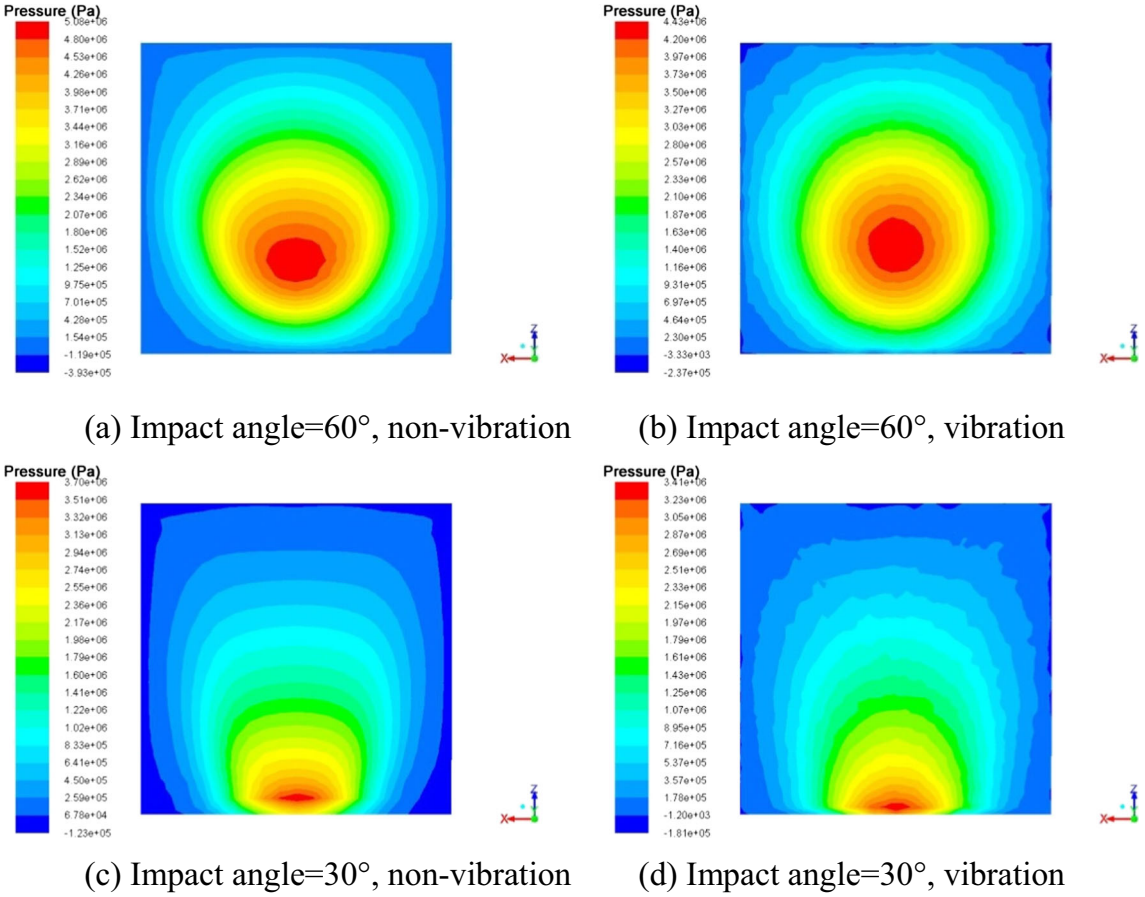

(a) Impact angle=60°, non-vibration (b) Impact angle=60°, vibration

(c) Impact angle=30°, non-vibration (d) Impact angle=30°, vibration

Fig. 9 Pressure distributions of flow fields on impacted surfaces under different impact angles. **a** Impact angle = 60°, non-vibration. **b** Impact angle = 60°, vibration. **c** Impact angle = 30°, non-vibration. **d** Impact angle = 30°, vibration

2.2 Boundary conditions

The impact of particle causes removal of target material and consumes certain amount of kinetic energy. Particles will rebound from the surface after the impact, and the retainment of kinetic energy can be characterized by coefficient of restitution. Coefficients of restitution define the ratio of momentum after and before the impact in normal and tangential direction, which can be defined as

$$e_n = \frac{v_{2,n}}{v_{1,n}} \tag{6}$$

$$e_t = \frac{v_{2,t}}{v_{1,t}} \tag{7}$$

where v_n is the normal component of particle velocity, v_t is the tangential component of particle velocity, and the subscripts 1 and 2 refer to before and after the impact, respectively. In the present simulation, the coefficients are set as functions of actual impact angle of particle as proposed by Grant and Tabakoff [22]:

$$e_n = 0.993 - 1.76\alpha + 1.56\alpha^2 - 0.49\alpha^3 \tag{8}$$

$$e_t = 0.988 - 1.66\alpha + 2.11\alpha^2 - 0.67\alpha^3 \tag{9}$$

where α is the actual impact angle of particle.

The particles driven by the fluid flow will impact on the workpiece surface and lead to material failure. The amount of removed material can be represented by erosion rate at the wall boundary, which is defined as

$$R_{erosion} = \sum_{p=1}^{N} \frac{c\dot{m}_p f(\alpha) v_p^b}{A_{face}} \tag{10}$$

where N is the number of particles, $\dot{m}_p$ is the mass flow rate of particles, c is a coefficient depending on target and abrasive material properties, $f(\alpha)$ is a function of impact angle, v_p is the particle velocity, b is the exponent relevant to particle velocity, and A_{face} is the area of cell face at wall boundary.

For brittle materials such as glass and ceramics, the common failure mode induced by abrasive erosion is fracture or crack. However, the formulation and propagation of fracture will not occur and the material failure will show ductile characterization with the premise of lower particle

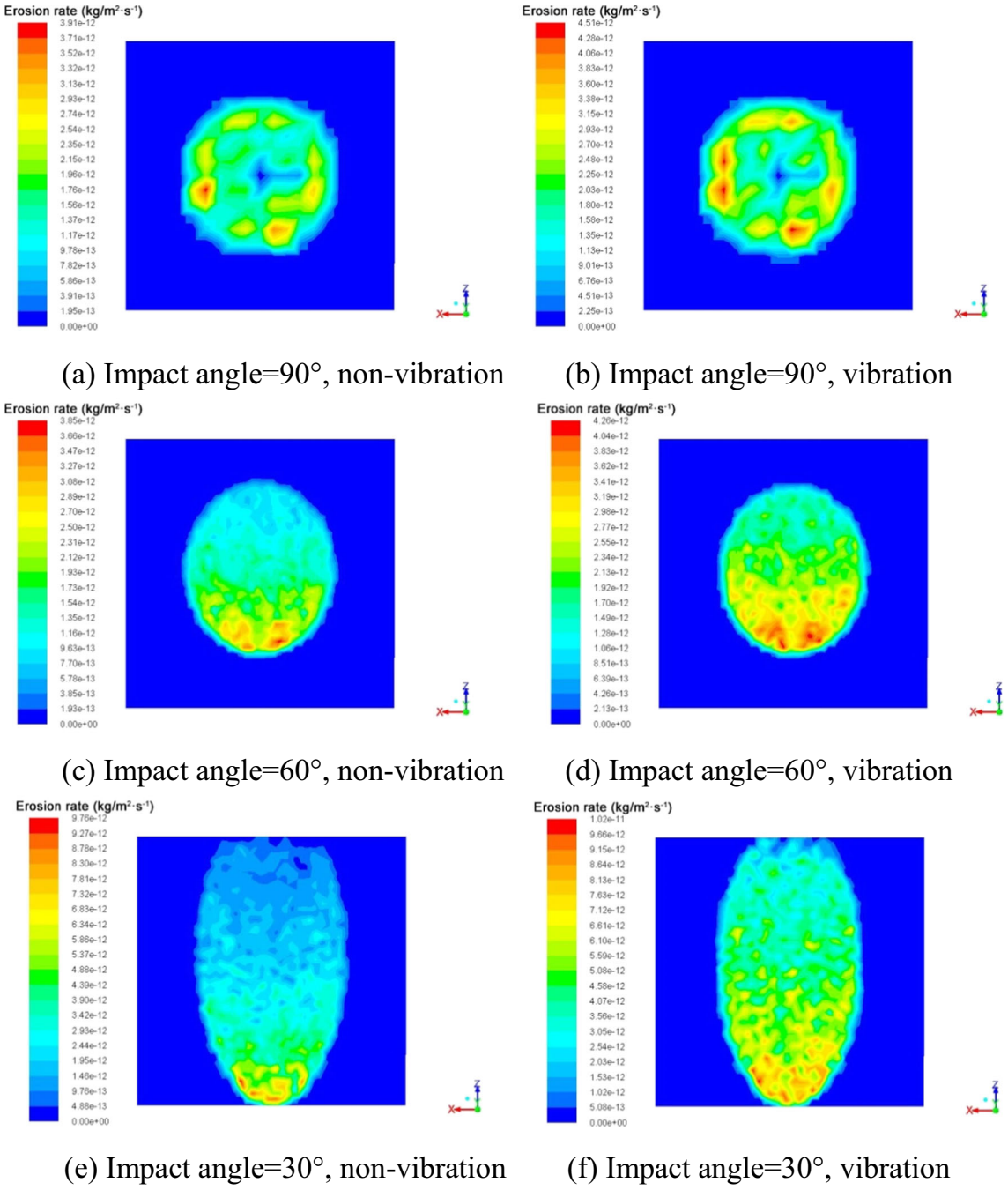

Fig. 10 Erosion rates on the impact surfaces under different conditions. **a** Impact angle = 90°, non-vibration. **b** Impact angle = 90°, vibration. **c** Impact angle = 60°, non-vibration. **d** Impact angle = 60°, vibration. **e** Impact angle = 30°, non-vibration. **f** Impact angle = 30°, vibration

kinetic energy [23]. In the present study, the parameters such as water pressure, particle diameter, and focusing tube diameter are determined according to previous researches on fine-abrasive waterjet ductile machining of brittle materials [13]. Therefore, the material removal mode can be considered as ductile in the present simulation. Based on the prediction model of erosion rate in [24], the exponent of particle velocity in Eq. (10) is chosen as 2 and the angle dependence can be expressed as follows:

$$\begin{cases} f(\alpha) = \sin(2\alpha) - 3\sin^2\alpha, & \tan\alpha \le 1/3 \\ f(\alpha) = \cos^2\alpha/3, & \tan\alpha > 1/3 \end{cases} \tag{11}$$

The obtained erosion rate model was evaluated by the experimental results in [13] and showed a fine coincidence as depicted in Fig. 1.

The geometry of computational domain of flow field is established in FLUENT 14.5 and shown in Fig. 2. The two-phase (air-water) flow enters the domain from the focusing

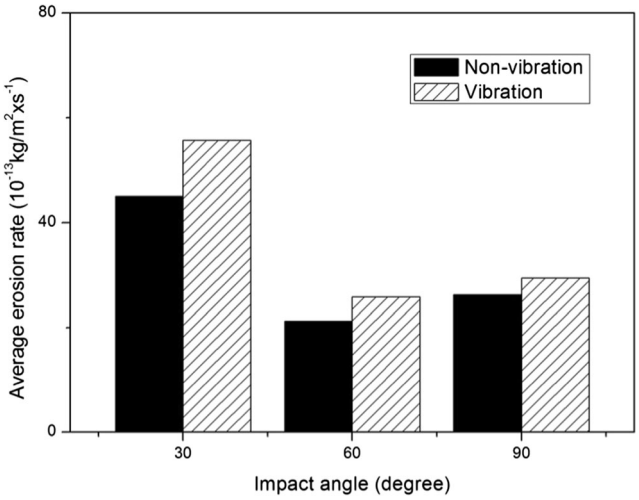

Fig. 11 The average erosion rates on impacted surfaces under different conditions

tube which is modeled as a pressure inlet. The pressure value at the inlet is 100 MPa, and the diameter of the focusing tube is 0.76 mm. Abrasive particles are mixed with the flow as the discrete phase. The average diameter of particles is 20 μm, and the flow rate is 0.1 g/s. The outer boundary of the domain is set as the pressure outlet of air with a pressure of standard atmosphere. The backflow was set as zero, indicating that deflected waterjet can go through the boundary. The workpiece surface was set as reflecting wall with a standoff distance of 5 mm to the focusing tube. The coefficients of particle moment restitution on target surface are set according to Eqs. (8) and (9). The erosion rate caused by discrete phase was calculated on the wall boundary during the impact process of jet flow based on Eq. (10). The vibration of workpiece surface in ultrasonic assisted abrasive waterjet machining was simulated by motivating the wall boundary. The direction of motion is perpendicular to the jet impact velocity, and the movement can be depicted as

$$\frac{dz}{dt} = 2\pi f A \cos 2\pi f t \tag{12}$$

where f and A are vibration frequency and amplitude, respectively. A user-defined function was compiled to realize the motion according to Eq. (12). The dynamic mesh was allocated at the adjacent area of moving wall to adjust the distortion. In the present simulation, the vibration frequency and amplitude are set as 20 kHz and 20 μm corresponding to the experimental parameters.

The domain geometry was partitioned with several blocks to realize the structural meshing. Models with the same meshing strategy but different total element numbers were established to select an appropriate mesh density. The meshed models were used to calculate flow field quantities under the same working parameters. It was found from the comparison result that the deviation of calculated maximum velocity is only 2.6% when the element number increases from 242,432 to 3,628,646. Therefore, the element number of 242,432 was used in simulation for ensuring the calculation accuracy and improving the efficiency. The meshed model is shown in Fig. 3.

3 Results and discussion

Figure 4 shows the flow structure of impinging abrasive waterjet. It can be found that the flow enters the computational domain with a high velocity and decreases along with the distance to inlet. This course is involved with the entrainment of ambient air and formation of swirl at the boundary layer and is accompanied by the increase of jet flow diameter. As the jet impinges the target surface, the flow is resisted and forms the

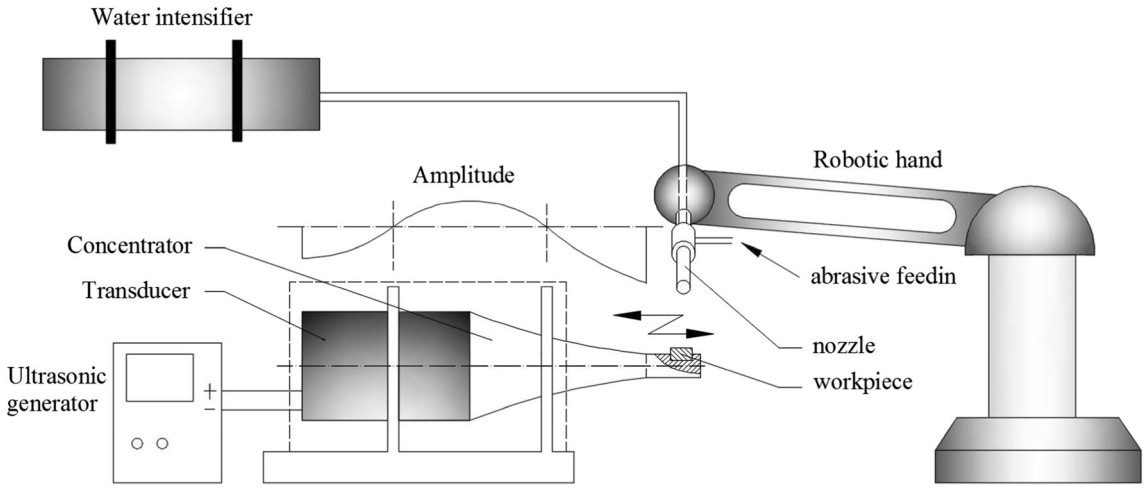

Fig. 12 Apparatus for ultrasonic assisted abrasive waterjet machining [13]

lateral flow spreading on the surface. As shown in Fig. 5, a water film with high pressure zone exists at the center of the impact area. Due to the stagnation effect of the water film, the velocity of following jet flow decreases when approaching the target and then gradually increases along the tangential direction away from the center. The particle tracks are shown in Fig. 6. As calculated by using discrete phase model, the trajectories of particles follow the streamlines and the velocity have similar variation trend with that of fluid field.

The impact erosion of workpiece material induced by particles is calculated based on Eq. (10) and is shown in Fig. 7. The erosion rate at center area of impacted zone is lower than that at peripheral area. This can be attributed to the fact that the velocities of particles near the centerline of jet flow are reduced by stagnation effect. Moreover, the impact direction of particle is deflected by the back flow and the actual impact angle is deviated from the perpendicular impact of jet flow. At peripheral area, the impact angle is lower and more suitable for ductile removal of material as depicted in [25]. With the spreading of lateral flow, the velocity of particle decreases and resulted in a reduction of erosion rate at the marginal area.

Figure 8 illustrates the pressure distribution of flow field on impacted surface at different time in a vibration period T. It is indicated that at $t = 0$, the maximum pressure value is 5.07 MPa; at $t = T/4$, the pressure increases to 5.37 MPa; and at $t = T/2$, pressure decreases to 5.02 MPa, which is similar to the value at $t = 0$. This variation is related to the motion of workpiece as described by Eq. (12). At $t = 0$, workpiece moves along the tangential direction and the vibrating velocity is at maximum value. The motion of surface affects the stagnation zone due to the shear at the interface layer of impact flow field. Vibrating velocity decreases as the motion of workpiece and turns to zero at $t = T/4$. The shear effect of workpiece surface is negligible, and thus, the pressure is almost equal to that under non-vibration condition. At $t = T/2$, the velocity magnitude of workpiece increases and therefore the pressure at stagnation zone decreases as a consequence of enhanced shearing of surface.

Figure 9 shows the pressure distribution of impact flow field on workpiece surface under different impact angles. It is indicated that the pressure value decreases with a reduction of impact angle. This is because of that the back flow formed on surface under lower impact angle is weaker than that under normal impact. Therefore, the stagnation effect is reduced with a decrease of impact angle.

Figure 10 shows the erosion rate on workpiece surface under different conditions. It is indicated that the erosion rate is higher under vibration condition. When the workpiece vibrates, the high-pressure water film at stagnation zone is affected and the resistance on momentum of impacting particle is reduced. As a consequence, the material removal is enhanced under vibration condition.

The average erosion rate at the impact surface is calculated and shown in Fig. 11. At the impact angle of 30°, the erosion rate obtained under vibration condition is 23.7% higher than that under non-vibration condition. At the impact angle of 90°, the erosion rate is only 12.2% higher under vibration condition. This can be attributed to that the ductile removal of impact erosion is more significant at nearly 30° impact angle. Therefore, the enhanced shear at the workpiece surface induced by tangential vibrating motion can lead to a higher increase of erosion rate.

In order to verify the results acquired through simulation, a series of ultrasonic vibration-assisted abrasive waterjet erosion experiments were implemented. The levels of process parameters were selected corresponding to those utilized in simulation. The apparatus is developed earlier by the present authors [13] and illustrated in Fig. 12. It mainly consists of a set of abrasive waterjet machining system and an ultrasonic stage which transmitting vibration to the workpiece. Aluminum substrates and silicon carbide powders were utilized as workpiece and abrasives, respectively. Mechanical properties of

Table 1 Properties of aluminum nitride

Properties	
Density [g/cm^3]	3.3
Vickers hardness [GPa]	12
Young modulus [GPa]	310
Flexural strength [MPa]	330
Fracture toughness [MPa·m$^{1/2}$]	3.2

Table 2 Properties of the silicon carbide

Composition [%]		Density [g/cm^3]	Vickers hardness [GPa]
SiC	Fe_2O_3		
> 97.5	< 0.7	3.2	31

Table 3 Main experimental parameters

Parameters	
Vibration frequency [kHz]	20
Vibration amplitude [μm]	19.8
Vibration power output [W]	1600
Nozzle diameter [mm]	0.76
Water pressure [MPa]	100
Abrasive diameter [μm]	20
Impact angle [°]	30, 60, 90
Stand-off distance [mm]	5
Abrasive feed rate [g/s]	1
Duration time of ejection [s]	1

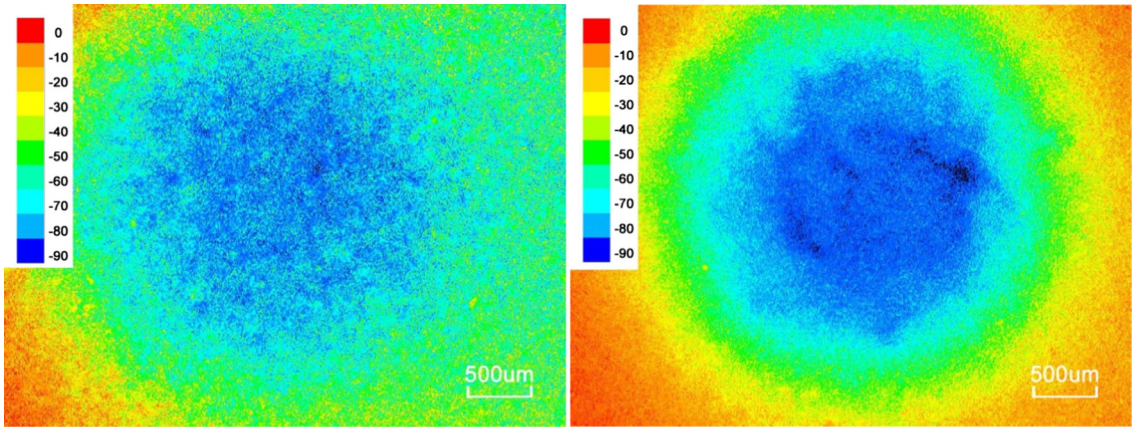

(a) Without vibration (b) With vibration

Fig. 13 The morphologies of erosion area created by abrasive waterjet with and without target vibration (impact angle = 90°). **a** Without vibration. **b** With vibration

workpiece and abrasive materials are listed in Tables 1 and 2, respectively. Some main experimental parameters are listed in Table 3. The surfaces of aluminum specimens were cleaned before and after the erosion in order to obtain the accurate removal amount.

The micrographs of eroded surfaces were obtained using laser scanning microscope and shown in Fig. 13. The surfaces are represented in the form of height contours which can distinctly indicate the erosion depth. It can be observed that the patterns are similar with those acquired by the corresponding simulations under the same conditions. The depth of erosion crater is higher when vibration is added. The volume of material removal can be measured in the postprocessor in attached soft packages of microscope. Due to the fact that the amount of material removal is too tiny to precisely measure by using electronic balance, the eroded mass is calculated by the product of density and the removed volume. The eroded mass in corresponding simulation trail can be calculated as follows:

$$m_{sim} = \int_{A_e} R_{erosion} dA \cdot t_e \tag{13}$$

where $R_{erosion}$ is the erosion rate, dA is the area of mesh face at target surface which is equal to A_{face}, A_e is the whole area of eroded zone, and t_e is the erosion time. The comparison between simulation and experimental results is shown in Fig. 14. It is indicated that the maximum of deviation is 19% and the agreement is acceptable.

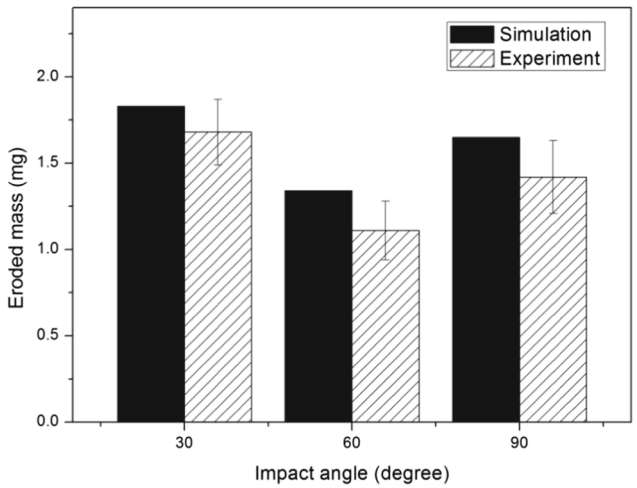

(a) Without vibration

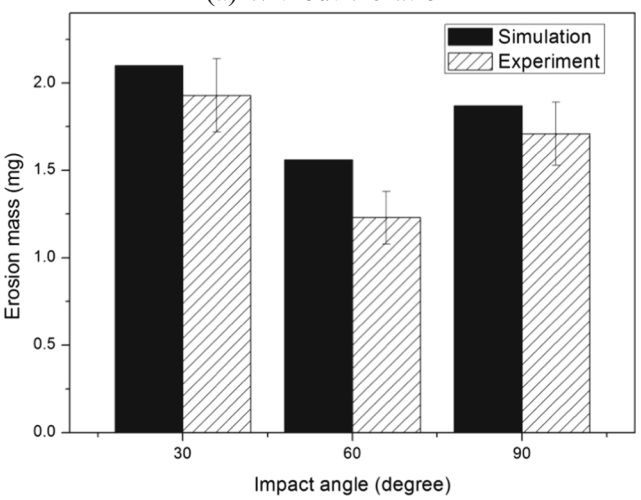

(b) With vibration

Fig. 14 Comparison of experimental and simulation results (error bars represent standard deviation). **a** Without vibration. **b** With vibration

4 Conclusions

A CFD-based model was established to study the flow field characteristics and particle erosion in ultrasonic vibration-assisted abrasive waterjet machining. The results indicated that the erosion rate at center area of impacted zone is lower than that at peripheral area, which is owing to the influence of

stagnation zone. The variation of pressure value at the impacted surface is related to the vibrating movement of workpiece. The maximum pressure value is relatively lower at $t = 0$ and $t = T/2$ than that at $t = T/4$. Due to the weakening of stagnation effect, the pressure value decreases with a reduction of impact angle. Moreover, it was found that the erosion rate induced by particle impact on target surface is increased when vibration is applied. This can be attributed to the influence of workpiece vibration on stagnation zone. The influence of ultrasonic vibration on erosion rate is more significant at lower impact angle, and thus, the increase of erosion rate obtained under vibration condition at 30° impact angle is higher than that at 90° impact angle. The simulation results were verified by the corresponding experiments and the comparison indicated an acceptable agreement.

Acknowledgements This work is supported by the National Natural Science Foundation of China (51405274).

Publisher's Note Springer Nature remains neutral with regard to jurisdictional claims in published maps and institutional affiliations.

References

1. Liu D, Zhu H, Huang C, Wang J, Yao P (2016) Prediction model of depth of penetration for alumina ceramics turned by abrasive waterjet—finite element method and experimental study. Int J Adv Manuf Technol 87:2673–2682. https://doi.org/10.1007/s00170-016-8600-x
2. Yue Z, Huang C, Zhu H, Wang J, Yao P, Liu Z (2014) Optimization of machining parameters in the abrasive waterjet turning of alumina ceramic based on the response surface methodology. Int J Adv Manuf Technol 71:2107–2114. https://doi.org/10.1007/s00170-014-5624-y
3. Wang JM, Gao N, Guo WJ (2010) Abrasive waterjet machining simulation by SPH method. Int J Adv Manuf Technol 50:227–234. https://doi.org/10.1007/s00170-010-2521-x
4. Finnie I (1960) Erosion of surfaces by solid particles. Wear 3:87–103. https://doi.org/10.1016/0043-1648(60)90055-7
5. Evans AG, Gulden ME, Rosenblatt M (1978) Impact damage in brittle materials in the elastic-plastic response regime. Proc R Soc London, Ser A 361:343–365. https://doi.org/10.1098/rspa.1978.0106
6. Sheldon GL, Finnie I (1966) On the ductile behaviour of nominally brittle materials during erosive cutting. J Eng Ind 88B:387–392. https://doi.org/10.1115/1.3672666
7. Zhu HT, Huang CZ, Wang J, Li QL, Che CL (2009) Experimental study on abrasive waterjet polishing for hard-brittle materials. Int J Mach Tools Manuf 49:569–578. https://doi.org/10.1016/j.ijmachtools.2009.02.005
8. Hou R, Huang C, Zhu H (2017) Experimental study on pulsation behavior of the ultrasonic vibration-assisted abrasive waterjet. Int J Adv Manuf Technol 91:3851–3859. https://doi.org/10.1007/s00170-017-0011-0
9. Peng Y, Wu YB, Liang ZQ, Guo YB, Lin X (2010) An experimental study of ultrasonic vibration-assisted grinding of polysilicon using two-dimensional vertical workpiece vibration. Int J Adv Manuf Technol 54:941–947. https://doi.org/10.1007/s00170-010-2991-x
10. Liang Z, Wang X, Wu Y, Xie L, Liu Z, Zhao W (2012) An investigation on wear mechanism of resin-bonded diamond wheel in elliptical ultrasonic assisted grinding (EUAG) of monocrystal sapphire. J Mater Process Technol 212:868–876. https://doi.org/10.1016/j.jmatprotec.2011.11.009
11. Li C, Zhang F, Meng B, Liu L, Rao X (2017) Material removal mechanism and grinding force modelling of ultrasonic vibration assisted grinding for SiC ceramics. Ceram Int 43:2981–2993. https://doi.org/10.1016/j.ceramint.2016.11.066
12. Xiao X, Zheng K, Liao W, Meng H (2016) Study on cutting force model in ultrasonic vibration assisted side grinding of zirconia ceramics. Int J Mach Tools Manuf 104:1–10. https://doi.org/10.1016/j.ijmachtools.2016.01.004
13. Lv Z, Huang C, Zhu H, Wang J, Wang Y, Yao P (2015) A research on ultrasonic-assisted abrasive waterjet polishing of hard-brittle materials. Int J Adv Manuf Technol 78:1361–1369. https://doi.org/10.1007/s00170-014-6528-6
14. Lv Z, Huang C, Zhu H, Wang J, Yao P, Liu Z (2015) FEM analysis on the abrasive erosion process in ultrasonic-assisted abrasive waterjet machining. Int J Adv Manuf Technol 78:1641–1649. https://doi.org/10.1007/s00170-014-6768-5
15. Qi H, Wen D, Lu C, Li G (2016) Numerical and experimental study on ultrasonic vibration-assisted micro-channelling of glasses using an abrasive slurry jet. Int J Mech Sci 110:94–107. https://doi.org/10.1016/j.ijmecsci.2016.03.013
16. Nouraei H, Kowsari K, Samareh B, Spelt JK, Papini M (2016) Calibrated CFD erosion modeling of abrasive slurry jet micro-machining of channels in ductile materials. J Manuf Process 23:90–101. https://doi.org/10.1016/j.jmapro.2016.06.007
17. Kowsari K, Nouraei H, Samareh B, Papini M, Spelt JK (2016) CFD-aided prediction of the shape of abrasive slurry jet micro-machined channels in sintered ceramics. Ceram Int 42:7030–7042. https://doi.org/10.1016/j.ceramint.2016.01.091
18. Qi H, Wen D, Yuan Q, Zhang L, Chen Z (2017) Numerical investigation on particle impact erosion in ultrasonic-assisted abrasive slurry jet micro-machining of glasses. Powder Technol 314:627–634. https://doi.org/10.1016/j.powtec.2016.08.057
19. Nouraei H, Wodoslawsky a, Papini M, Spelt JK (2013) Characteristics of abrasive slurry jet micro-machining: a comparison with abrasive air jet micro-machining. J Mater Process Technol 213:1711–1724. https://doi.org/10.1016/j.jmatprotec.2013.03.024
20. Kowsari K, Nouhi A, Hadavi V, Spelt JK, Papini M (2017) Prediction of the erosive footprint in the abrasive jet micro-machining of flat and curved glass. Tribol Int 106:101–108. https://doi.org/10.1016/j.triboint.2016.10.038
21. Qi H, Xie Z, Hong T, Wang Y, Kong F, Wen D (2017) CFD modelling of a novel hydrodynamic suspension polishing process for ultra-smooth surface with low residual stress. Powder Technol 317:320–328. https://doi.org/10.1016/j.powtec.2017.05.030
22. Kowsari K, Amini MH, Papini M, Spelt JK (2016) The effects of fluid vapor pressure and viscosity on the shapes of abrasive slurry-jet micro-machined holes and channels. Int J Mach Tools Manuf 110:80–91. https://doi.org/10.1016/j.ijmachtools.2016.09.004
23. Sheldon GL, Finnie I (1966) The mechanism of material removal in the erosive cutting of brittle materials. J Eng Ind 88:393–399. https://doi.org/10.1115/1.3672667
24. Finnie I (1995) Some reflections on the past and future of erosion. Wear 186–187:1–10. https://doi.org/10.1016/0043-1648(95)07188-1
25. Finnie I, Stevick GR, Ridgely JR (1992) The influence of impingement angle on the erosion of ductile metals by angular abrasive particles. Wear 152:91–98. https://doi.org/10.1016/0043-1648(92)90206-N